2017

Automated methods for the quantification of 3D woven architectures

Amanda J. Levinson
U.S. Naval Research Laboratory

David J. Rowenhorst
U.S. Naval Research Laboratory, david.rowenhorst@nrl.navy.mil

Keith W. Sharp
Saertex USA, LLC.

Stephen M. Ryan
Johns Hopkins University

Kevin J. Hemker
Johns Hopkins University

See next page for additional authors

Materials Characterization 124 (2017) 241–249

Contents lists available at ScienceDirect

Materials Characterization

journal homepage: www.elsevier.com/locate/matchar

Automated methods for the quantification of 3D woven architectures

Amanda J. Levinson[a], David J. Rowenhorst[a,*], Keith W. Sharp[b], Stephen M. Ryan[c], Kevin J. Hemker[c,d], Richard W. Fonda[a]

[a] U.S. Naval Research Laboratory, Materials Science and Technology Division, Washington, DC 20375–4000, USA
[b] Saertex USA, LLC., 2200-A Mt. Holly-Huntersville Road, Huntersville, NC 28078–9338, USA
[c] Department of Materials Science and Engineering, Johns Hopkins University, 3400 N Charles Street, Baltimore, MD 21218, USA
[d] Department of Mechanical Engineering, Johns Hopkins University, 3400 N Charles Street, Baltimore, MD 21218, USA

ARTICLE INFO

Article history:
Received 23 August 2016
Received in revised form 3 January 2017
Accepted 5 January 2017
Available online 6 January 2017

Keywords:
Serial sectioning
3D woven structure
Characterization

ABSTRACT

Serial sectioning was used to characterize the three-dimensional (3D) architecture of metallic textiles, a new class of periodic cellular materials for structural applications. Reconstructing the serial sectioned data required the development of an adaptive stitching algorithm to montage individual tiles from each section due to the sparse nature of this periodic structure where a predefined stitching pathway does not perform well. This dataset was used to develop computational tools to automate the quantification of the bonding efficiency and weave geometry to inform the weave processing as well as incorporate these parameters in the development of material models for more accurate performance prediction. An inverse correlation was present between the wire spacing and the bonding efficiency of wire joints where bonding efficiency increased with a decrease in wire spacing. These tools could have broader applications analyzing other periodic cellular materials, containing similar sized struts, utilizing different materials or processing routes.
Published by Elsevier Inc.

1. Introduction

The manufacture and optimization of cellular materials is a broad field that has produced new material architectures with unique combinations of mechanical, permeability, thermal, and acoustic properties that show promise as heat exchangers, filters, actuators, and porous bone implant scaffolds [1,2]. Three-dimensional (3D) metallic textiles are a unique class of multifunctional periodic cellular materials that can achieve exceptional combinations of strength and permeability [3]. While many periodic cellular structures are engineered to possess a high specific strength, the absolute magnitudes of their strength are quite low owing to their low density [4,5]; woven metallic textiles, however, can maintain a high degree of permeability with a higher average density and thus more structural stability [6]. These advanced textile techniques, which include 3D braiding, 3D weaving, and 3D knitting [7–9], were originally developed to manufacture complex, near-net-shape preforms for composites that were not susceptible to the delamination problems inherent in conventional laminated forms [10]. These techniques have been extended to the fabrication of 3D structures from metallic (or even a combination of metallic and non-metallic) wires and/or yarns. This paper will discuss a specific textile structure, the non-crimp 3D weave structure (see Fig. 1a), which consists of alternating perpendicular layers of warp and fill wires that are held together by Z wires.

Topology optimization has proven to be an invaluable tool for designing structures with an optimized strength-to-weight performance. Zhao et al. [3] and Zhang et al. [6] have shown that the permeability and stiffness of these weaves can be improved significantly through a combination of topology optimization to increase the open architecture of the weave and bonding strategies to join the wire junctions and strengthen the woven structure. A number of bonding strategies including vapor phase deposition [11,12], soldering [13], and brazing [3], have all shown success in joining these woven structures.

3D characterization of the weave structure is essential to accurately assess the resultant weave topology and bonding characteristics. Variations within woven textiles have led to significant changes in property measurements [14–16]. This makes the characterization of 3D woven textiles paramount for accurate model development and validation, as well as providing feedback to help improve the manufacturing process. Because 3D characterization generates a massive amount of information about the structure, the associated tasks of manual data collection, image segmentation, 3D reconstruction, and quantitative analysis can be extremely time-consuming. Development of automated reconstruction techniques and quantification algorithms can enable analyses of much larger

* Corresponding author.
E-mail address: david.rowenhorst@nrl.navy.mil (D. Rowenhorst).

http://dx.doi.org/10.1016/j.matchar.2017.01.005
1044-5803/ Published by Elsevier Inc.

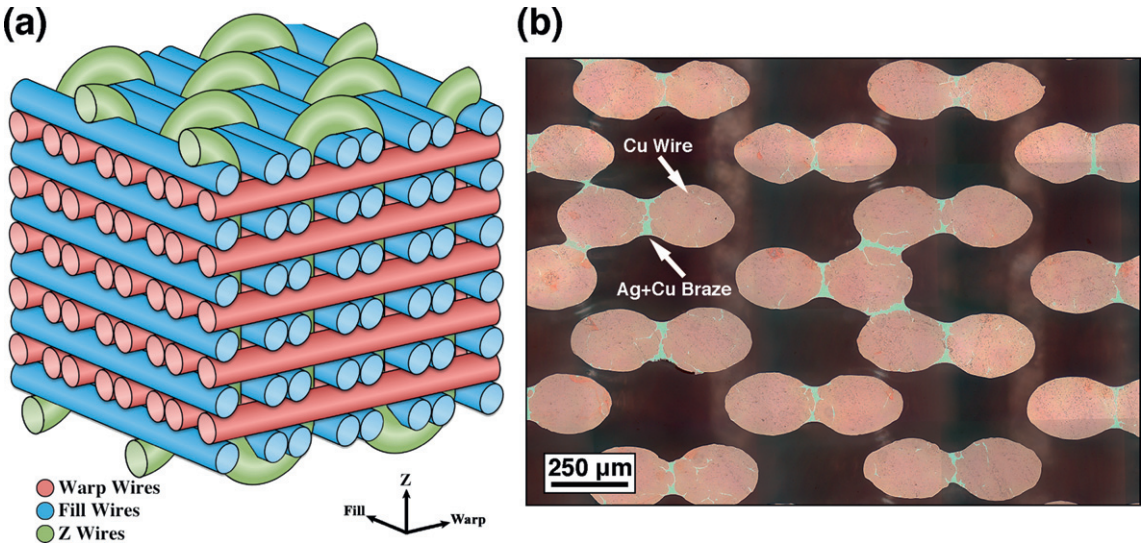

Fig. 1. (a) Schematic of the 3D orthogonal weave architecture with pairs of non-crimp warp (red) and fill (blue) wires crossing at 90° with Z wires (green) woven through the thickness and bent over the outermost fill layers. (b) Optical micrograph of the cross-section of fill and warp wires at 45° showing the distinction between the copper wires appearing red and the Ag-Cu braze appearing gray in the image.

datasets in a timely fashion, yielding more accurate evaluations of the measurements and their distributions within these structures. This paper will present such algorithms that were developed to automate the reconstruction and quantification of a non-crimp 3D weave structure. It is important to note that while these automated reconstruction and quantification techniques were developed for this specific non-crimp 3D weave structure, these algorithms are applicable to a much broader range of materials and structures containing similarly sized struts.

2. Material

The non-crimp 3D weaves [17] were fabricated by 3TEX using 202 μm copper wires. A schematic of the woven structure is shown in Fig. 1a. The weave contains three wire types, labeled as warp, fill and Z wires. The warp and fill wires are deposited as wire pairs aligned perpendicular to each other on alternating layers, with a total of five warp layers and six fill layers. The Z wires are woven through the thickness orthogonal to the other two wire types, but are also bent around the outermost fill wires to bind the structure together. In this study, all the wires were copper with the same diameter, although different materials and wire diameters have been used to increase the application space of these structures. Wire junctions within the woven structure were bonded together by placing two brazing foils of the eutectic Ag–Cu composition (72 wt.% Ag, 28 wt.% Cu) above and two foils below the weave and heating to 900 °C for 5 min. Further details of this procedure can be found in [3]. The final structure contained a mass gain of 15% braze. An optical micrograph of the weave after brazing, with the copper wires and Ag–Cu braze clearly delineated, is shown in Fig. 1b. In this image the warp and fill wire pairs are oriented at 45° to the image plane, causing the cross sections of the cylindrical wires to appear as ellipses.

3. Data collection

The 3D structure of this brazed copper weave was revealed by serial sectioning, which can acquire high resolution microstructural data from a large volume. Serial sectioning involves collecting a series of two-dimensional images, typically a few hundred, on consecutive parallel planes and then aligning those images in the third dimension to produce a 3D representation of the structure. The serial sectioning was performed using a Robo-Met.3D fully automated serial sectioning system manufactured by UES on a brazed copper weave sample oriented about 45° from the warp wire direction that had been mounted in epoxy to prevent wire deformation and fall-out. The section height for each slice was approximately 10 μm, accomplished through a two step mechanical polish: 10 min using a 3 μm diamond solution and then an additional 10 min with 1 μm diamond solution, with both steps using a 20 N load and a 150 RPM wheel speed. Each section was imaged by optical microscopy using a Zeiss Axio Observer using a 20X/0.5 NA objective, but in order to achieve the desired high resolution across each 15.5 mm × 3 mm section, the surface was imaged as a montage of 189 individual images on a 27 × 7 grid with an overlap between neighboring images of 10%. Each tile was 1292 × 968 pixels as a RGB image with 8-bits per color channel, with a pixel size of 0.5 × 0.5 μm^2. A total of 350 sections were collected, for a total analyzed volume of 15.5 mm × 3.5 mm × 3 mm. The time to collect this dataset was approximately eight days.

4. Reconstruction

Creating an accurate 3D reconstruction from the serial sectioning data is critical for correctly quantifying the characteristics of that structure; therefore, care must be taken to ensure that both the image of each sectioned plane and the reconstructed volume accurately reflect the original structure. In this study, generation of an accurate 3D reconstruction of the brazed copper weave involved three primary steps: (1) stitching together the individual image tiles from each section into a single montaged image, (2) aligning each montaged image with those from the other sections, and (3) segmenting the images to identify the locations of the copper and braze constituents.

While conventional stitching algorithms usually perform well at assembling image montages from individual image tiles that have shared features in the overlapping regions, the open architecture of this weave sometimes resulted in a lack of discernable image features in the overlapping regions. This can prevent standard stitching algorithms that follow a pre-determined path for combining

neighboring image tiles from properly placing those images. Therefore, an adaptive stitching algorithm with a flexible assembly path was developed that only incorporates images into the final montage as overlapping information becomes available. An example of this procedure is shown in Fig. 2a, using four neighboring image tiles. The overlapping region between image tiles 1 and 2 does not contain shared data (i.e. no wire or braze material), and would not be placed properly using a conventional stitching algorithm. By comparison, the new adaptive stitching algorithm would only place an image tile in position if the overlapping regions share common data. The incorporation of a new image tile in the montage is only allowed when there is sufficient shared data between overlapping regions, as evaluated by the maximum value of the cross-correlation between these regions. Cross-correlation is a measure of the similarity between two functions, and can be used in image processing to align images using their common features [18,19]. A threshold was applied to the maximum value of the cross-correlation to determine if the overlapping region between two images contained shared data. The threshold value was chosen a priori by evaluating the cross-correlation of overlapping regions on many neighboring tiles. Using this methodology on the example in Fig. 2a, the maximum value of the cross-correlation between image tiles 1 and 2 would fall below the threshold and these images would not be stitched. Instead, assembly of the image montage would progress from image 1 through image tiles 3, 4, and then 2, all of which contain shared data, to join image tiles 1 and 2. This adaptive algorithm was able to correctly montage all 189 image tiles in each of the 350 sections. A complete image montage from one section is shown in Fig. 2b.

The alignment between images along the third dimension is critical for an accurate reconstruction of the 3D structure. This alignment was performed in two steps: an initial correction using cross correlation of the image features followed by use of an external standard. An additional alignment of the image orientation is also usually necessary, but was not needed for this study due to the rotational accuracy of the Robo-Met.3D custom kinematic sample holders. The initial alignment maximizes the cross-correlation between adjacent sections to determine the x–y translational shift that minimizes the displacement of features between sections. This cross-correlation can be efficiently computed at all spatial locations in Fourier space despite the large (approximately 710 MB) size of each image. However, using the image features as an internal alignment standard can prevent an accurate reconstruction of the 3D structure if there is any preferred alignment of those features. For example, because cross correlation minimizes the displacement of features between sections, it will stack images of an inclined feature directly on top of one another rather than in its actual inclined orientation. Similarly, use of the cross correlation generated translational alignment errors because the warp and fill wires had slightly different orientations. To address this, a known static feature – the sample clip placed around the weave prior to mounting, shown on the left in Fig. 2b – was used as an external standard to refine the alignment. This was accomplished through maximization of the cross-correlation of the sample clip features. The elongated shape of the sample clip was not effective for aligning the images in the vertical direction, so this feature could not be used for a single step alignment of the image stack. However, the sample clip provided a particularly good reference point for corrections in the horizontal direction, where the translational errors from the inclined warp and fill wires were largest. Thus, when combined with the initial alignment, this additional step provided a very accurate alignment of the images.

After all of the slice-to-slice alignments were recorded, the images were then stacked to form the 3D volume. While using the high resolution 2D images was useful for perfecting the stitching and alignment of the images, using the full $31,000 \times 6000$ pixel image with three bytes per pixel to store the color information would result in a 3D volume that consumed 195 GB of computational memory. This investigation is primarily interested in the degree of bonding between wires, thus much lower resolution images are sufficient. For the final stacking of images, each 2D image is aligned, then down-sampled using a bilinear interpolation to 3100×600 pixels (equivalent to 5μ m/pixel), providing the final reconstruction with a voxel size of $5 \times 5 \times 10\,\mu m^3$. While this resolution is not sufficient to capture the fine details of the braze-wire interfaces, it is sufficient to detect if the wires have significant contact patches between them. The fully reconstructed volume, composed of 350 sections, is shown in Fig. 3.

The final step in reconstructing the 3D volume is to identify the locations of the copper wires and braze. Segmentation of the Cu wires, Ag–Cu braze, and epoxy matrix (background) was accomplished by thresholding using distinctions between the colors and brightness of each feature. Fig. 4 shows the processed histogram of the red, green, and blue color channels with the corresponding feature of each peak (matrix, wire or braze) indicated. First the color values were shifted so that the location of the dark matrix peak in the histogram occurred at the same brightness for all color channels. Since the peaks from the braze are superimposed on the tail of the large copper wire peak, the color channels were stretched so that the peak for the copper wires occurred at the same brightness for all color channels, thereby setting a large difference in the values of the blue and red channels of the minority braze phase (see inset in Fig. 4).

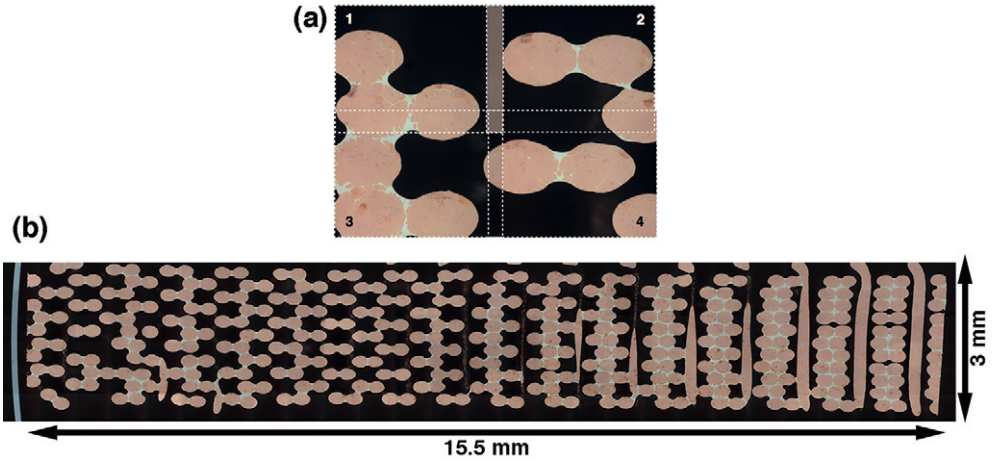

Fig. 2. (a) An illustration of the new adaptive stitching algorithm using four neighboring image tiles with overlapping regions (white dashed outlines). The algorithm compensates for the lack of shared features between tiles 1 and 2 by stitching tiles 1 and 3, then tile 4, and finally tile 2. (b) Optical micrograph of a full 2D section composed of a grid of 27×7 image tiles (189 images total) encompassing an area of 15.5mm×3mm.

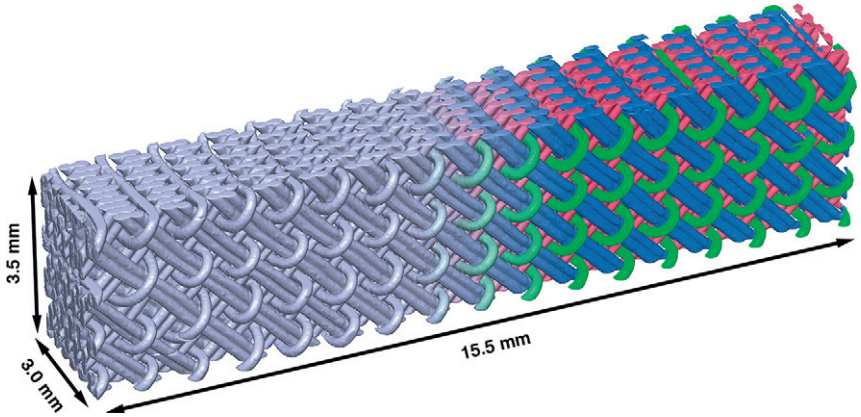

Fig. 3. Reconstruction of the 3D serial sectioned dataset collected on the copper weave composed of 350 sections with a total volume of 15.5mm×3.0mm×3.5mm. The three wire types are indicated with red = warp, blue = fill, and green = Z.

A simple threshold was applied to segment the epoxy matrix from the solid phases (both wires and braze) due to the large separation of their corresponding peaks in the histogram. A second threshold was then applied to segment the wires and braze by taking the difference between the blue channel and the red channel of the solid phases. Pixels that had a small difference between the two channels were labeled as copper wire, while those with a large difference were labeled as braze. A final cleanup procedure was applied to remove any single pixel noise. A typical image of the brazed weave after segmentation is shown in Fig. 5a.

5. Quantification

5.1. Wire labeling

In order to quantify aspects of the woven structure, such as the bonding efficiency and wire spacings, the wires need to be individually labeled. The procedure used to label the wires is shown in Fig. 5. After the initial segmentation of the matrix, wire, and braze components (Fig. 5a), the Cu wires were eroded to separate the individual wires from each other. This was performed by applying an appropriate threshold on a 3D Euclidean distance map of the segmented Cu wires. The Euclidian distance map creates a mapping where the value of each pixel is equivalent to the distance from that pixel to the closest interface. Applying a threshold to the Euclidian distance map is equivalent to repeated erosion operations. Here, an erosion threshold of 60 μm was determined to be appropriate for this structure by tracking the number of wire regions as the structure was sequentially eroded. This amount of erosion was well beyond the initial increase in the number of wire regions caused by the separation of individual wires from their neighbors, but remained below the level at which further eroding caused the individual wires to break up. The resulting wire cores were labeled with unique identifiers, as illustrated in Fig. 5b. Using these labeled wire cores as seed regions, a watershed algorithm was applied to the original distance map which was based on the Cu wire interface. This effectively dilated the labeled wire cores out until they impinged on their nearest neighbors domains using a watershed algorithm, which generated a map in wherein every pixel, including pixels in the matrix and braze regions, were labeled according to the closest wire core (Fig. 5c). While it may appear to be preferable to use the weave (wire or braze)–epoxy interface to define the distance map used for the erosion and dilation operators, it was found that using the weave–epoxy interface leads to a less well defined threshold for the erosion operator, and a higher number of false interfaces in the watershed/dilation operator. Furthermore, the interfaces that were properly labeled using the weave-epoxy distance maps in the watershed/dilation operator had nearly identical positions as compared to when using the distance maps created from the Cu wire interfaces. Finally, the map was masked with the original structure (Fig. 5a) to uniquely label each wire and its associated braze within the structure, as shown in Fig. 5d.

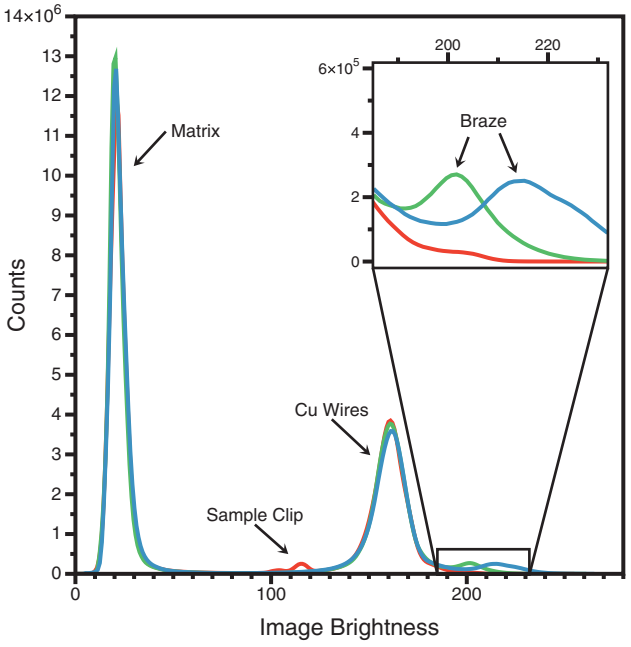

Fig. 4. Brightness histogram of each color channel over a single 2D section. Individual peaks representing the matrix, sample clip, and Cu wires are labeled. Inset shows close-up of the region containing the braze, with peaks in the green and blue histogram comprising the braze.

The wire type (either fill, warp, or Z) of each wire within the structure was identified by its predominant orientation. This was accomplished by fitting an ellipsoid to each wire, calculating the inertial tensor, and then determining the eigenvalues and eigenvectors, which represent the magnitudes and directions of the ellipsoid axes. The orientation of the wire axis, corresponding to the eigenvector with the maximum eigenvalue, was used to identify wires oriented along the warp or fill directions. Wires that were not oriented along either of these directions were classified as Z wires. Fig. 3 shows the results of this classification, in which different colors are used to identify each wire type.

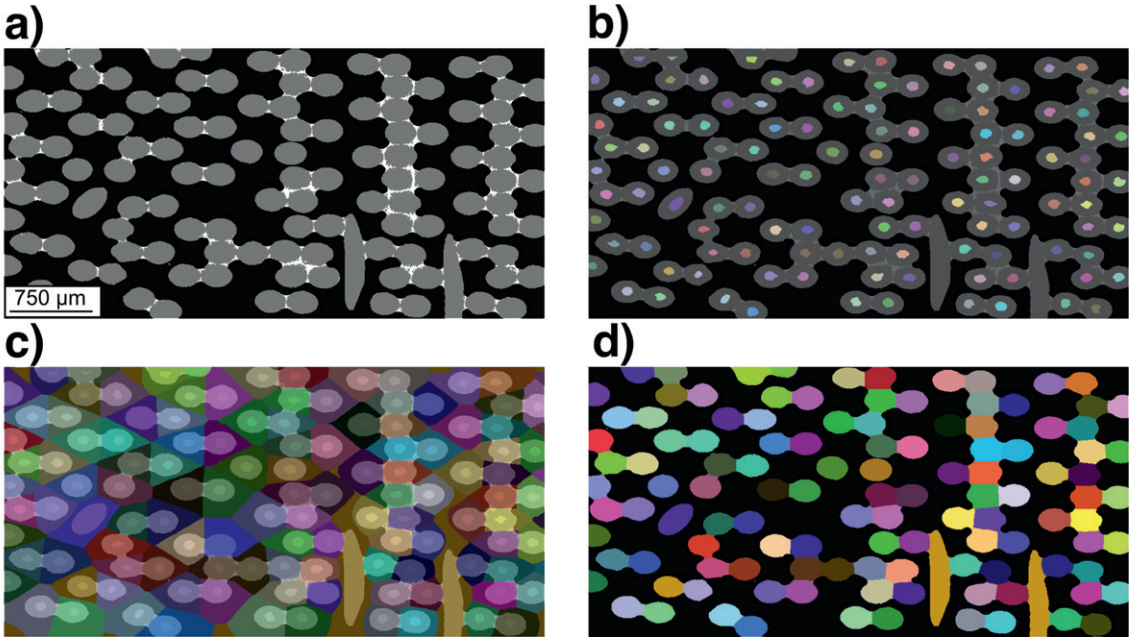

Fig. 5. Wire segmentation algorithm illustrated on part of a 2D section (algorithm was applied to the full 3D structure). (a) Initial segmentation of the matrix (black), wires (gray), and braze (white). (b) Identification of the wire cores. (c) Watershed subdivision of all regions to closest wire core. (d) Masking with original structure (wire and braze) to reveal segmented wires, each with a unique identifier.

5.2. Bonding

Achieving superior combinations of properties, such as improved stiffness and permeability, in woven textiles is dependent on the ability to place bonding material only at wire joints and thus maintain the open architecture of the structure. To determine the effectiveness of different bonding strategies, the bonding efficiency was evaluated over a statistically significant number of wire joints. The local and global bonding efficiencies, along with a quantitative evaluation of the spatial separation of wires within the woven structure, is critical to both inform and validate finite element simulations for performance predictions.

This investigation is interested in determining if two wires that pass close to each other have a bond, and if they are bonded what is the approximate cross-sectional area of that bonded region. In order to evaluate the bonding efficiency at a statistically significant number of wire intersections, a new algorithm was developed to automatically determine whether two wires were bonded or not. This algorithm determines the location of the closest approach between the two wires from a 3D signed distance map computed between from the interface of the weave (wire or braze) and epoxy matrix. This methodology is illustrated in Fig. 6 with a 2D example containing three idealized wire cross-sections, two of which are bonded to each other and one that is not bonded to another wire, along with their associated watershed regions as discussed in Section 5.1. A signed Euclidean distance map is computed so that each pixel (or voxel) is labeled with the distance to the closest interface between the solid phases (wire or braze) and the epoxy matrix. This distance is represented as the height (z-axis) in Fig. 6b,c, with a value of zero along the interface between the solid phases and the matrix, positive values inside the solid weave, and negative values in the matrix. The closest approach between two wires can then readily be determined by identifying the maximum value of this distance map within the boundary between the two watershed regions. If the maximum value is positive, then the two wires are touching and assumed to be bonded, as illustrated in Fig. 6c by the black dot at the maximum of the blue–red interface. If instead the maximum value along the watershed domain interface is negative, then the wires do not touch each other and thus are not bonded, as shown in Fig. 6c by the white dot occurring at the maximum of the blue–green interface. In this case, the absolute value of the distance function at the maximum point is half the distance between the two non-contacting wires at their closest approach.

In the case where there are only two contacting wires within a bond, the value of the positive distance function would be an indication of the bond size. However, in the more general case wherein more than two wires are contacting within a bond, the maximum value of the distance map would not provide an accurate measure of the bond size between any two wires that occur in the bond region. Thus, the cross-sectional size of the bonded region between a wire pair was estimated by fitting an ellipsoid to the locations of the voxels along the interface between the two regions that have positive values in the distance map (thus voxels that contain wire or braze along the interface). This ideally forms a disk two voxels thick that are along either side of the interface between the two wire pairs, and the two major axes of the 3D ellipsoid are representative of the contact patch between the two bonded wires/braze. Here the bond size was taken as the average of the two major axes of the ellipsoid. It is important to note that this bonding algorithm combines relatively common image processing techniques (distance mapping and watershedding) in a unique way to quantify the bonding efficiency, bond size and wire separation, which can be applied to other periodic cellular structures with uniform size struts.

5.3. Wire spacing

Quantifying the spacing between the constituent wires, as well as the variations in those spacings, is critical for an accurate characterization of the structure. In addition, accurate wire spacing data is essential for the development and validation of performance models for these woven structures. We therefore developed an algorithm to automate the calculation of wire spacing distributions in these woven textiles. This information is important to correlate with the bonding efficiency since bonding is inherently dependent on the wire spacing. When brazing the woven structures, the braze distribution and bond formation are strongly dependent on the capillary

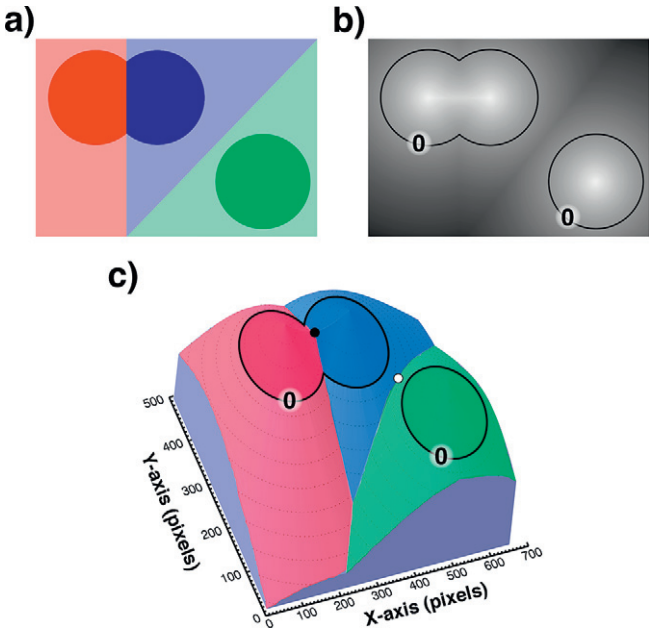

Fig. 6. Example of the bond algorithm illustrated using a) three wire/braze cross-sections in 2D, labeled as described in Section 5.1. b.) Grayscale signed distance map of the weave–epoxy matrix interface, and c) a 3D contour map of the signed distance map where the original boundary, set to be the zero distance is marked by the black lines. Distances within the wire/braze region are considered positive, distances within the epoxy matrix are considered negative. The dots indicate the maximum value of the distance map along the boundary between two neighboring regions. Contacting wires will have a positive value at their maximum value (black dot) while non-contacting wires will have a negative value at their maximum value (white dot), with the magnitude of the value of the distance map being the half the distance of closest approach of the two wires.

attraction of the melted braze to the wire joints, which is a function of the wire spacing.

The wire spacings were calculated from two-dimensional slices taken perpendicular to the average orientation of each wire type. The warp and fill wire types were segmented following the procedure outlined in Section 5.1 to generate a 3D dataset for each wire type. (The spacing between Z wires was not calculated due to the large curvature of those wires and the associated variation in inter-wire spacings.) Two-dimensional slices of the wire cross-sections were obtained by slicing the 3D dataset perpendicular to the average orientation of the component wires. Next, the centroid of each wire cross-section was assigned as the midpoint of its x- and y-coordinates. A Delaunay triangulation was then used to identify the distances to the neighboring wire centroids. Fig. 7 shows an example of this algorithm applied to an idealized two-dimensional plane containing wire cross-sections. The Delaunay triangulation provides a connectivity list showing the distance from each point to its closest neighbors (i.e. the wire spacings), corresponding to the spacing between the wire centroids. These calculations were limited to wires located in the same row or column by thresholding the value of the dot product of each vector with the horizontal and vertical axes. Running this algorithm on many slices through the structure (using the same plane normal) provides a statistically significant number of wire spacings for an accurate quantification of the individual wire spacing distributions.

6. Results and discussion

The methods discussed above were used to determine the bonding efficiencies and bond sizes in the woven structure. The 3D volume, shown in Fig. 3, contained 439 individual wires (230 fill wires, 189 warp wires, and 20 Z wires). The bonding efficiencies between the warp-fill, fill-Z, and warp-Z wire pairs were computed using the algorithm discussed in Section 5.2 to be 92.5%, 61.4%, and 29.7% respectively. At least some of this variation can be attributed to the different environments of each bond type originating from the manufacturing process. The high bonding efficiency between the warp and fill wires reflects the compression of the structure by the Z wires. The fill and Z wires were also compressed during manufacturing, but these wires were not held in that position. Instead they were allowed to relax between compressions by the reed, the tool used as a spacer to separate the warp wires and bend the Z wires, resulting in a lower bonding efficiency. The poor bonding between the warp and Z wires arises primarily from the inherent reed spacing, which allows for a larger gap between these wires.

The size of each bond, represented by the equivalent circular radius of the bond area, is shown in Fig. 8. This demonstrates that the warp-fill wire junctions are well bonded with a substantial bond area. The equivalent circular radius of these bonds is approximately 100 μm. Bonding between the Z wires and either the warp or fill wires, however, is significantly worse. Both the bonding efficiency (61.4% with fill, 29.7% with warp) and bond areas (see Fig. 8) are substantially below those observed for the warp-fill bonds. The bonding efficiency and the bond size determinations are of great importance in modeling the mechanical properties of these structures as they control the geometry and thus the properties of the load transfer points and are highly dependent on the bond type in this architecture. These results are being incorporated into FE simulations of the woven structures.

Fig. 9 shows the distributions of calculated spacings between wire classes using the method described in Section 5.3. As mentioned above, the Z wire spacings were not calculated due to the curvature of these wires, but the measurements of the warp and fill spacings provide some information on the Z wire spacings. The various spacings that were measured are illustrated in Fig. 9a. The wire pair spacing (Fig. 9b) corresponds to the spacing between the two parallel wires in a wire pair. The layer spacing (Fig. 9c) corresponds to the through-thickness spacing between a specific warp or fill wire and the corresponding wire of the same type located directly above or below. Thus, this spacing also includes the distance across the intervening layer of the other wire type. The Z spacing (Fig. 9d) reflects the in-plane spacing between warp wires or fill wires that are separated by a Z wire insertion. The mean and standard deviation of each wire spacing are shown in Table 1.

A surprising aspect of the wire pair spacings (Fig. 9b) is that they extend significantly below the 202 μm diameter of the wires, the limit where two wires would be in direct contact. Fill wire pairs were observed with spacings of 190 μm, and warp wire pair spacings extended nearly down to 160 μm. This is likely a result of the brazing process. During the brazing heat treatment it was observed that not only does the braze melt but it also diffuses into the copper wires and the edges of the wires begin to dissolve. To better understand this process, a sample was prepared that fully immersed a weave in a braze pool. The solidified structure was analyzed in a Zeiss Versa 520 X-ray computed micro-tomography system, possessing a voxel size of $0.7 \times 0.7 \times 0.7 \mu m^3$. Fig. 10 shows a 2D slice through the 3D reconstructed tomograms, showing two warp wire pairs bounded by two Z wires. Braze is represented as the lighter phase in Fig. 10. The cross-sections of the wires are no longer circular but have braze penetrating along the grain boundaries of the copper wires and copper dendrites that have re-precipitated within the braze region. At the brazing temperature of 900 °C, copper has extensive solubility in the 28% copper:72% silver braze, accounting for the observed penetration of the braze into the wire structure. In this case there was an overabundance of braze used, and thus a large portion of the wire–braze interface was dissolved. In the serial-sectioned sample, a minimal amount of braze was used and is more evenly distributed

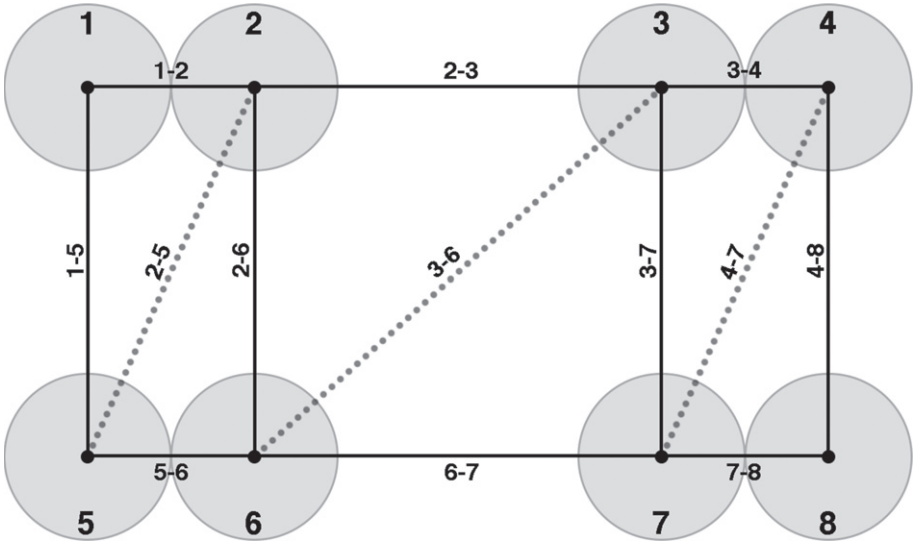

Fig. 7. Schematic illustrating wire spacing computed on a two-dimensional cross-section using the Delaunay triangulation of the centroids of each wire. The connectivity between the nodes used to compute the spacing between neighboring wires are shown with solid lines while the other connected nodes produced from the Delaunay triangulation, not used in the computation, are shown with dashed lines.

with the capillarity forces causing it to gather near the wire junctions, and thus there is less dissolution of the wire interface. The resolution of the serial-sectioning process is not sufficient to reveal the fine details of this dissolution process at each bond, but nonetheless, it appears that the braze reacted with the copper wires during the brazing process, partially liquifying the wire surface and allowing capillary forces to draw the wires closer together than the spacing of two solid contacting wires.

The distributions of the layer spacing for warp and fill wires (Fig. 9c) are very similar as they measure essentially the same characteristic spacing — the diameter of two wires (one warp and one fill) and twice the open space between the warp wire layer and the fill wire layer. The average spacing between adjacent layers of the same wire type (warp or fill) is 414 μm. This corresponds to an average distance of 207 μm for each wire layer through the thickness of the weave, and thus a gap of approximately 5 μm on either side of the 202 μm wires in that direction. This small interwire spacing, which is a testament to the high quality of the weaving process, enables the high bonding efficiency observed between the warp and fill wires (92.5% efficiency), as these small gaps would not take much braze to fill and would possess high capillarity forces.

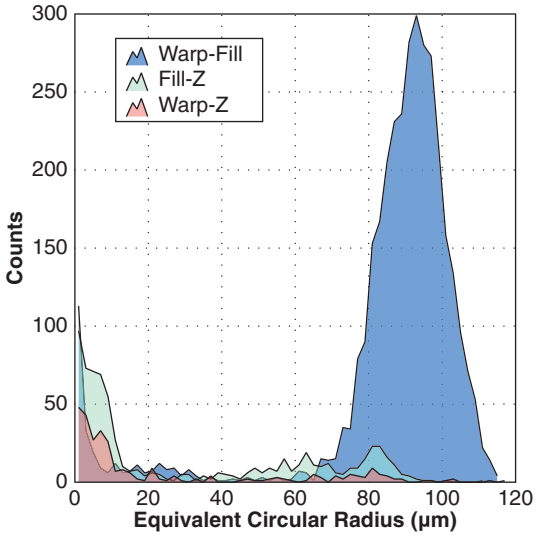

Fig. 8. Plot of the number of joints versus the equivalent circular radius of the bond area representing the distribution of the bond areas for the fill-warp, fill-Z and warp-Z joints.

The average Z spacing for the fill and warp wires has the broadest distribution of the measured spacings — at least twice as wide as the next broadest spacing (see Table 1). The average spacings of 469 and 506 μm for the fill-Z and warp-Z wire junctions correspond to average gaps of 32.5 and 51 μm, respectively, between the adjacent wire surfaces. These gaps correlate with the lower (61.4% and 29.7%) bonding efficiencies of these wire intersections, with larger interwire gaps resulting in lower bonding efficiencies between those wires. As mentioned above, the moderate packing between the fill and Z wires was likely caused by compression of the reed during the weaving process. After insertion of each set of fill wires, the reed presses against those wires to consolidate the weave, compressing the fill and Z wires together. Alternatively, the reed spacing defines the separation between the warp and Z wires. These wires must flow freely through the reed during weave fabrication, and the larger reed gap spacing required to accomplish this is reflected in a larger warp-Z spacing.

The algorithm described in Section 5.2 was used to calculate the probability of bonding between wire types, and Fig. 11a demonstrates that the bonding efficiency is inversely related to the average gap between wires for each bond type. The average gap between the constituent wires in the warp-fill, fill-Z, and warp-Z joints increases from 5 μm to 32.5 μm and then 51 μm, respectively, accompanied by a decrease in bonding efficiency from 92.5% to 61.4% and then 29.7%. Further analysis of the probability of bonding two wires with a specific wire separation (Fig. 11b) was performed. This was evaluated using a variation of the algorithm for computing bonding efficiency (Section 5.2), wherein the separation distances were calculated using the distance map from only the Cu wire interfaces (not including the braze), thereby providing an estimate of the original distance between the wires before adding the braze (this is a simplification, because as discussed above the braze pull the wires closer at bonded regions), while the presence of a bond was evaluated using both the Cu wire and braze.

The resultant trends are shown in Fig. 11b. The full dataset contained 8305 potential wire junctions, 74% of these were categorized having Cu wires in direct contact even without the braze, which

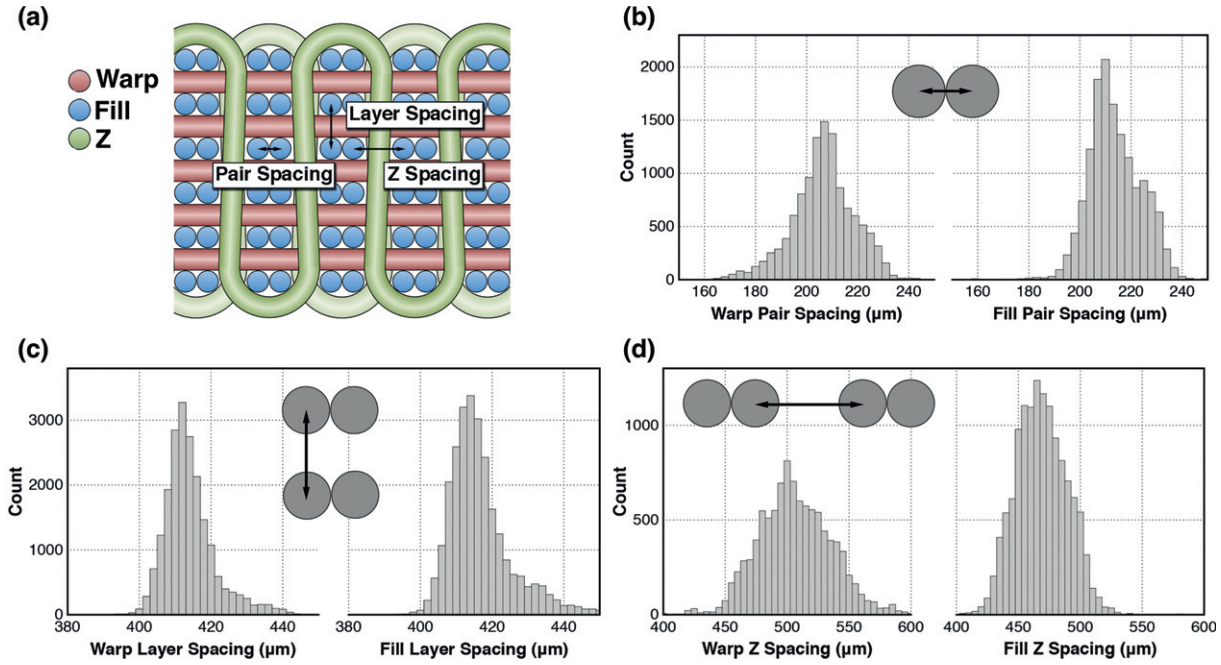

Fig. 9. Distribution of wire spacings. (a) Schematic indicating the corresponding spacing measurements. The distribution of wire spacings between (b) wire pairs, (c) layers of wires and (d) and Z wires.

may be due in part to the surface melting and capillarity-driven wire attractions discussed above. Of the remaining 26% (2184) of wire junctions, the addition of braze only produced additional bonding at 100 junctions. This plot shows that there is a very steep decline in the bonding efficiency with increasing wire separation as the bonding probability of all wire pairs at a separation distance of less than 10 μm is only at 15%. With gap spacings greater than 10 μm the bonding probability is less than 5%. This demonstrates the need for a high-quality weaving process such as the 3D non-crimp weaving process used in this study to manufacture structures with consistently small wire separations to be able to strengthen those structures through brazing of the wire junctions.

7. Conclusions

This paper presents algorithms that were developed to automate various stages in the reconstruction and quantification of 3D woven textile structures, but which are also applicable to a variety of other periodic cellular materials. A large 3D volume of this woven metallic textile (15.5 mm× 3.0 mm× 3.5 mm), composed of 202 μ m copper wires bonded with a Ag–Cu braze, was collected using serial sectioning and reconstructed into a segmented 3D volume. High resolution within each section was achieved with optical microscopy, but required development of an adaptive stitching algorithm to handle montaging of images with sparse shared data. These 2D images and the segmented 3D reconstruction revealed significant diffusion of the Ag–Cu braze into the copper wires and formation of copper dendrites within the braze material, obscuring some of the original domains of each copper wire. Additional algorithms were developed to segment wires, quantify the closest approach between neighboring wires and compute wire spacings by combining commonly used image processing tools such as watershedding, distance transformations, and Delaunay triangulation.

Quantification of this woven metallic structure focused on determination of wire spacings and bonding efficiencies. The three bond types within this structure (warp-fill, fill-Z, and warp-Z) exhibited an inverse relationship between bonding efficiency and wire spacing with bonding efficiencies of 92.5%, 61.4% and 29.7% corresponding to average gap spacings of 5.5, 32.5, and 51 μm, respectively. Further analysis demonstrated that 74% of wire joints were bonded

Table 1
Mean and standard deviation for each wire spacing.

	Pair spacing (μm)	Layer spacing (μm)	Z spacing (μm)
Warp	206.5±12.16	414.1±7.09	506.2±29.23
Fill	213.7±10.24	416.6±8.69	468.8±20.50

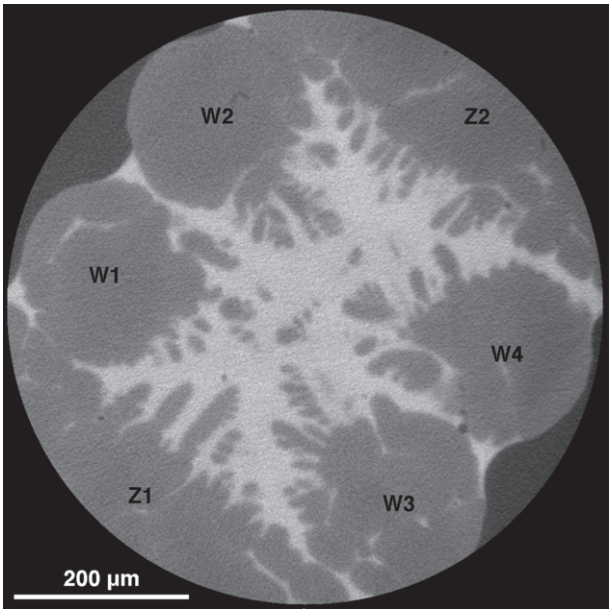

Fig. 10. Reconstructed slice from x-ray tomography scan of two sets of copper warp wires (labeled W1–W4) and two copper Z wires (labeled Z1 and Z2) bonded with the Ag–Cu braze. Ag–Cu braze is lighter gray and copper is darker gray. The braze infiltrates and partially melts the wires in the bonded regions.

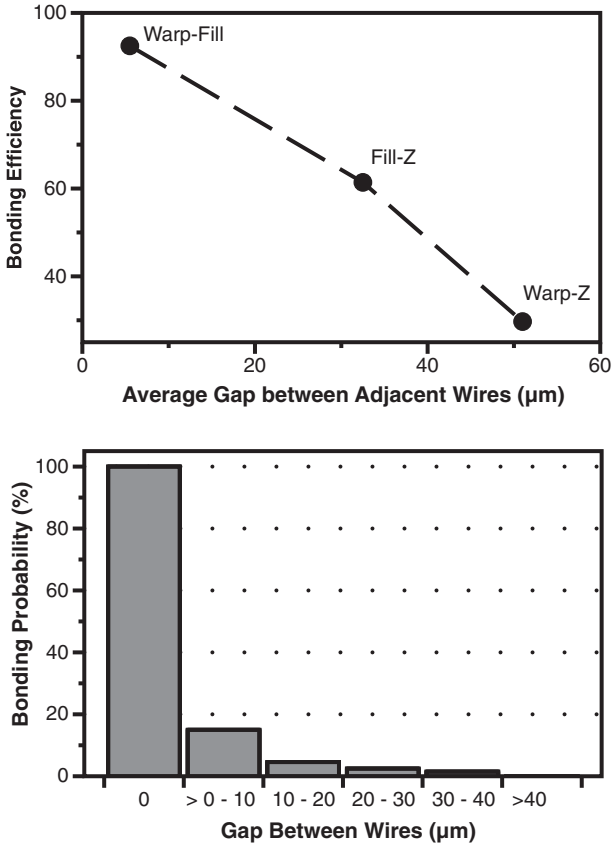

Fig. 11. (a) Average gap spacing between wire pairs versus the bonding efficiency measured as the percentage of bonded pairs for each pair type (warp-fill, fill-Z or warp-Z). (b) Probability of having two wires bonded by braze as a function of their gap spacing.

after the braze was removed; while the remaining bonding efficiency decreased rapidly such that wire spacings greater than 10 μm contained a bonding probability of less than 5%. The high quality of this 3D non-crimp woven structure was able to achieve an average bonding efficiency of 76%. Further work is needed to determine the optimal amount of braze that would result in a maximum bonding efficiency while maintaining the open architecture of the woven structure.

Acknowledgments

This work was funded by the Defense Advanced Research Projects Agency (DARPA)-Materials with Controlled Microstructural Architecture (MCMA), under award no. W91CRB1010004 (Dr. Judah Goldwasser, program manager).

References

[1] J. Banhart, Manufacture, characterisation and application of cellular metals and metal foams, Prog. Mater. Sci. 46 (6) (2001) 559–632.
[2] H. Wadley, Cellular metals manufacturing, Adv. Eng. Mater. 4 (10) (2002) 726–733.
[3] L. Zhao, S. Ha, K.W. Sharp, A.B. Geltmacher, R.W. Fonda, A.H. Kinsey, Y. Zhang, S.M. Ryan, D. Erdeniz, D.C. Dunand, K.J. Hemker, J.K. Guest, T.P. Weihs, Permeability measurements and modeling of topology-optimized metallic 3-D woven lattices, Acta Mater. 81 (2014) 326–336.
[4] M.F. Ashby, The mechanical properties of cellular solids, Metall. Trans. A 14 (9) (1983) 1755–1769.
[5] L.J. Gibson, Mechanical behavior of metallic foams, Annu. Rev. Mater. Sci. 30 (2000) 191–227.
[6] Y. Zhang, S. Ha, K. Sharp, J.K. Guest, T.P. Weihs, K.J. Hemker, Fabrication and mechanical characterization of 3D woven Cu lattice materials, Mater. Des. 85 (2015) 743–751.
[7] A.P. Mouritz, M.K. Bannister, P.J. Falzon, K.H. Leong, Review of applications for advanced three-dimensional fibre textile composites, Compos. A: Appl. Sci. Manuf. 30 (12) (1999) 1445–1461.
[8] M.H. Mohamed, A.E. Bogdanovich, L.C. Dickinson, J.N. Singletary, R.B. Lienhart, A new generation of 3D woven fabric preforms and composites, SAMPE J. 37 (3) (2001) 8–17.
[9] A.E. Bogdanovich, M.H. Mohamed, Three-dimensional reinforcements for composites, SAMPE J. 45 (6) (2009) 8–28.
[10] M.H. Mohamed, Z. Zhang, Method of Forming Variable Cross-Sectional Shape Three-Dimensional Fabrics, US Patent, 1992, 5085252. Feb 4
[11] D. Erdeniz, A.J. Levinson, K.W. Sharp, D.J. Rowenhorst, R.W. Fonda, D.C. Dunand, Pack aluminization synthesis of superalloy 3D woven and 3D braided structures, Metall. Mater. Trans. A 46 (1) (2015) 426–438.
[12] D. Erdeniz, K.W. Sharp, D.C. Dunand, Transient liquid-phase bonded 3D woven Ni-based superalloys, Scr. Mater. 108 (2015) 60–63.
[13] R.W. Fonda, M.J. Scherr, A.B. Geltmacher, Soldering a 3D wire lattice structure, J. Mater. Eng. Perform. 22 (11) (2013) 3376–3380.
[14] F. Desplentere, S.V. Lomov, D.L. Woerdeman, I. Verpoest, M. Wevers, A. Bogdanovich, Micro-CT characterization of variability in 3D textile architecture, Compos. Sci. Technol. 65 (13) (2005) 1920–1930.
[15] S.V. Lomov, I. Verpoest, T. Peeters, D. Roose, M. Zako, Nesting in textile laminates: geometrical modelling of the laminate, Compos. Sci. Technol. 63 (7) (2003) 993–1007.
[16] K. Hoes, D. Dinescu, H. Sol, R.S. Parnas, S. Lomov, Study of nesting induced scatter of permeability values in layered reinforcement fabrics, Compos. A: Appl. Sci. Manuf. 35 (12) (2004) 1407–1418.
[17] M.H. Mohamed, M.M. Salama, High Speed Three-Dimensional Weaving Method and Machine, US Patent, 2001, 6315007. Nov 13
[18] L.G. Brown, A survey of image registration techniques, ACM Comput. Surv. 24 (4) (1992) 325–376.
[19] B. Zitova, J. Flusser, Image registration methods: a survey, Image Vis. Comput. (2003)